

# An Extension of the Truncated Ingard-Myers Boundary Condition for High Mach Number Grazing Flows

Fang Q. Hu\*

*Old Dominion University, Norfolk, VA 23529, USA*

Douglas M. Nark†

*NASA Langley Research Center, Hampton, VA 23681-2199, USA*

The Ingard-Myers impedance boundary condition is widely recognized to be prone to hydrodynamic Kelvin-Helmholtz-type instability, primarily due to its use of a vortex sheet to model the flow at the boundary. Previously, a stabilized approximation of the Ingard-Myers condition, called the Truncated Ingard-Myers Impedance Boundary Condition (TIMIBC), has been introduced. This approximation offers a good representation of the Ingard-Myers condition for grazing flows characterized by low to mid subsonic Mach numbers. This paper explores an extension of the TIMIBC, referred to as TIMIBC-ext, designed for liners in grazing flows with high subsonic Mach numbers. The TIMIBC-ext introduces a tunable parameter and demonstrates that by judiciously selecting the parameter value, the accuracy of the TIMIBC can be improved for either upstream or downstream propagating waves in grazing flows with high subsonic Mach numbers. Consequently, the TIMIBC-ext represents an enhancement to the TIMIBC when the location of the source relative to the liner (upstream or downstream) is known. Time domain implementations of the TIMIBC-ext are also provided, employing a multipole expansion model for the impedance function. A numerical example is provided to assess the performance of the TIMIBC-ext, comparing computational results with measurements from a recent set of measurements in the NASA Langley Grazing Flow Impedance Tube.

## I. Introduction

THE Ingard-Myers impedance boundary condition has often been employed as the limiting case of the boundary layer thickness approaching zero[1, 2]. Nevertheless, it is widely acknowledged that the Ingard-Myers condition is subject to the hydrodynamic Kelvin-Helmholtz-type instability due to its use of a vortex sheet in modeling the flow at the boundary[3, 4]. This instability becomes particularly problematic in numerical simulations of liners conducted in the time domain.

Recently, a stabilized approximation of the Ingard-Myers condition, called the Truncated Ingard-Myers Impedance Boundary Condition (TIMIBC), has been proposed[5, 6]. The TIMIBC formulation involves truncating the second derivative term present in the Ingard-Myers condition when expressed in terms of acoustic pressure and its normal derivative on the liner surface. Analytically, it was shown that the TIMIBC effectively eliminates the instability inherent in the original Ingard-Myers formulation. Additionally, for grazing flows characterized by low to mid subsonic Mach numbers, the TIMIBC was shown to provide a good approximation to the Ingard-Myers condition.

In the context of acoustic liners integrated within an engine nacelle, the grazing flows encountered at the liner surface may exceed the low Mach number regime. This paper aims to consider an extension of the TIMIBC to liners subjected to grazing flows characterized by high subsonic Mach numbers. To achieve this, a generalization of the TIMIBC is formulated with a tunable parameter, of which the TIMIBC is a special case. For convenience of discussion, this generalized condition will be referred to as the TIMIBC-ext. It will be demonstrated that by judiciously selecting the parameter value, the accuracy of the TIMIBC can be enhanced for either upstream or downstream propagating waves in grazing flows characterized by high Mach numbers.

Furthermore, a numerical simulation of a liner in a grazing flow is presented. The experimental setup used is the NASA Langley Grazing Flow Impedance Tube (GFIT)[7]. The inherently internal duct acoustic propagation problem is reformulated as an external scattering problem, which is then solved using the time domain boundary element method[5]. In the experiment, the centerline setpoint Mach number inside the duct is moderately high at 0.6, and the incident

---

\*Professor, Department of Mathematics and Statistics, AIAA Associate Fellow

†Senior Research Scientist, Applied Acoustics Branch, Research Directorate, AIAA Associate Fellow

plane wave is positioned downstream of the liner. In the simulation, the TIMIBC-ext, tuned for downstream sources, is applied as the boundary condition on the liner surface. Comparisons between computational results and experimental measurements are carried out to demonstrate the validity of the TIMIBC-ext.

The rest of the paper is organized as follows: In Section II, formulation of the TIMIBC-ext is given as a generalization of the TIMIBC and a stability condition is shown for the tunable parameter in the TIMIBC-ext. Section III assesses the potential benefits of the TIMIBC-ext formulation. Time domain implementation of the impedance boundary condition is discussed in Section IV. A numerical example is presented in Section V and concluding remarks are given in Section VI.

## II. Formulation of TIMIBC-ext

The Ingard-Myers condition written in terms of the acoustic pressure and its normal derivative is

$$\rho_0 \left( -i\omega + U \frac{\partial}{\partial x} \right)^2 \hat{p}(\mathbf{r}, \omega) = i\omega Z \frac{\partial \hat{p}(\mathbf{r}, \omega)}{\partial n} \quad (1)$$

where  $\hat{p}(\mathbf{r}, \omega)$  is the acoustic pressure,  $U$  and  $\rho_0$  are the velocity and density of the mean flow respectively, and  $Z$  is the surface impedance. Here, a time dependency of  $e^{-i\omega t}$  is assumed for the frequency domain solutions and  $\mathbf{r} = (x, y, z)$  denotes the position vector. The impedance boundary condition, Eq. (1), is applied at the surface of the liner which is assumed to be at  $z = 0$ . The normal derivative for  $\hat{p}(\mathbf{r}, \omega)$  is in the direction out of the fluid and into the liner. For convenience of discussion, it is assumed the mean flow is in the same direction as the  $x$  axis and  $U \geq 0$ .

It can be shown (see, e.g., Ref. [6]), that the Ingard-Myers impedance boundary condition, Eq. (1), leads to the following dispersion relation for the intrinsic linear waves of the form  $\hat{p}(\mathbf{r}, \omega) = A e^{ik_x x + ik_y y + i\gamma z - i\omega t}$ :

$$(\omega/c)\gamma Z + \rho_0 c (\omega/c - M k_x)^2 = 0 \quad (2)$$

where

$$\gamma = \sqrt{(\omega/c - M k_x)^2 - (k_x^2 + k_y^2)} \quad (3)$$

and  $k_x$  and  $k_y$  are the wave numbers in  $x$  and  $y$  directions respectively,  $M = U/c$  is the mean flow Mach number, and  $c$  denotes the speed of sound. The branch-cut in the complex  $\omega$  plane for the square-root function in Eq. (3) is such that

$$\text{Im} \left\{ \sqrt{(\omega - U k_x)^2 - c^2 (k_x^2 + k_y^2)} \right\} \geq 0. \quad (4)$$

It is well documented in the literature that the dispersion relation given in Eq. (2) can support instability waves (e.g., Ref. [3, 4]). That is, given real values of  $k_x$  and  $k_y$ , Eq. (2) entails roots for  $\omega$  with a positive imaginary part, i.e.,  $\text{Im}\{\omega\} > 0$ .

As an approximation to the Ingard-Myers condition, the TIMIBC proposed in Ref. [6] is formulated by truncating the second derivative term  $\rho_0 U^2 \frac{\partial^2 \hat{p}}{\partial x^2}$  when the operator  $\left( -i\omega + U \frac{\partial}{\partial x} \right)^2$  in Eq. (1) is expanded, yielding

$$\rho_0 \left( i\omega \hat{p} - 2U \frac{\partial \hat{p}}{\partial x} \right) = Z \frac{\partial \hat{p}}{\partial n}. \quad (5)$$

The truncation is not expected to cause large errors when  $U$  is small. More importantly, it eliminates the instability wave inherent in the Ingard-Myers condition. The TIMIBC (Eq. 5) leads to a new dispersion relation:

$$\gamma Z + \rho_0 c (\omega/c - 2M k_x) = 0. \quad (6)$$

It was shown in [6] that Eq. (6) contained no unstable roots for  $\omega$ . That is, given real values of  $k_x$  and  $k_y$ , Eq. (6) has no roots for  $\omega$  where  $\text{Im}\{\omega\} > 0$ .

The proposed extended formulation presented in this paper is a generalization of the TIMIBC (Eq. 5) as follows:

$$\rho_0 \left( i\omega \hat{p} - (1+s)U \frac{\partial \hat{p}}{\partial x} \right) = Z \frac{\partial \hat{p}}{\partial n} \quad (7)$$

where  $s$  is a tunable parameter. This impedance condition will be denoted as the TIMIBC-ext. The generalization is based on the mathematical properties of the dispersion relations, as will be detailed below. Clearly, the TIMIBC-ext (Eq.

7) recovers the TIMIBC (Eq. 5) when  $s = 1$ . It is straightforward to find that the dispersion relation for the TIMIBC-ext is

$$\gamma Z + \rho_0 c (\omega/c - (1+s)Mk_x) = 0. \quad (8)$$

It will be shown below that the TIMIBC-ext is stable for any choice of  $s$  under the condition

$$|sM| < 1. \quad (9)$$

To demonstrate stability, let the dispersion relation (Eq. 8) be rewritten as

$$\frac{\gamma}{(\omega/c - (1+s)Mk_x)} = -\frac{\rho_0 c}{Z}. \quad (10)$$

We note that the numerator of Eq. (10), where  $\gamma$  is as defined in Eqs. (3) and (4), has branch points at  $\omega/c = (M-1)k_x$  and  $\omega/c = (M+1)k_x$ , shown as points A and C in Fig. 1 (assuming  $k_y = 0$  and  $k_x > 0$ ). The denominator of Eq. (10) is a linear function of  $\omega/c$  and has a zero at  $\omega/c = (1+s)Mk_x$ , noted as point B in Fig. 1. Under condition (9), we have

$$M-1 < (1+s)M < M+1.$$

That is, point B will be located between the two branch points A and C in Fig. 1 when parameter  $s$  satisfies Eq. (9). It is easy to show that this is true for  $k_x < 0$  as well. Then, for any  $\omega$  on the upper half plane, denoted by point D in Fig. 1, we have

$$\arg \left\{ \frac{\gamma}{(\omega/c - (1+s)Mk_x)} \right\} = \frac{\alpha_1 + \alpha_2}{2} - \beta = \frac{\alpha_2 - \beta}{2} - \frac{\beta - \alpha_1}{2} = \frac{\theta_2}{2} - \frac{\theta_1}{2}, \quad (11)$$

for any real value of  $k_x$  and a subsonic Mach number  $M$ . Here, the angles for the arguments are as shown in Fig. 1.

Now considering triangles  $\triangle ADB$  and  $\triangle BDC$ , we obviously have

$$0 < \theta_1 < \pi, \quad 0 < \theta_2 < \pi. \quad (12)$$

Then, it follows immediately that

$$-\frac{\pi}{2} < \frac{\theta_2}{2} - \frac{\theta_1}{2} < \frac{\pi}{2}. \quad (13)$$

Hence,

$$-\frac{\pi}{2} < \arg \left\{ \frac{\gamma}{(\omega/c - (1+s)Mk_x)} \right\} < \frac{\pi}{2},$$

and

$$\operatorname{Re} \left\{ \frac{\gamma}{(\omega/c - (1+s)Mk_x)} \right\} > 0. \quad (14)$$

That is, for the left hand side of Eq. (10), it maps any value of  $\omega$  in the upper half of the complex  $\omega$  plane to a complex number whose real part is positive.

For the right hand side of Eq. (10), however, because of the passivity condition for the impedance function  $Z(\omega)$ , namely,  $\operatorname{Re} \{Z(\omega)\} \geq 0$  for  $\operatorname{Im}\{\omega\} \geq 0$ , it maps any value of  $\omega$  in the upper half of the complex  $\omega$  plane to a complex number whose real part is negative. as we have

$$\operatorname{Re} \left\{ -\frac{\rho_0 c}{Z} \right\} \leq 0. \quad (15)$$

Therefore, it follows that it is not possible for Eq. (10) to have a root in the upper half  $\omega$  plane, and the dispersion relation equation (Eq. 8) for the TIMIBC-ext will contain no unstable waves for any value of parameter  $s$  that satisfies condition (9).

The benefits of choosing a proper value for  $s$ , particularly for a high subsonic mean flow Mach number, are discussed next.

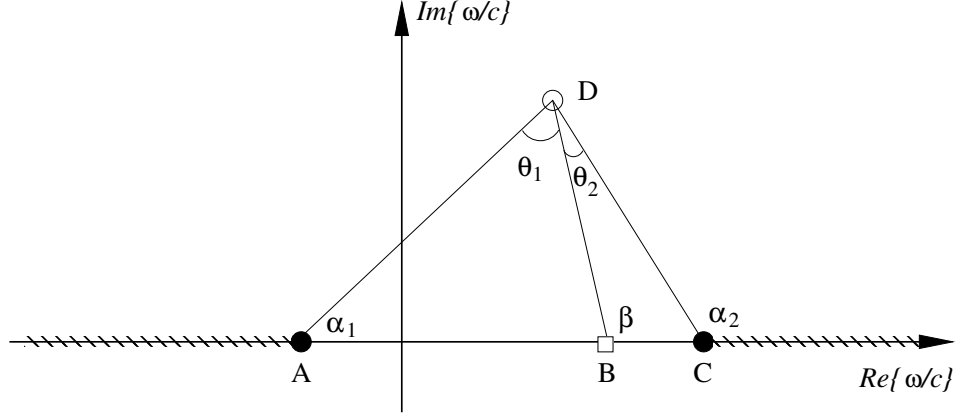


**Figure 1** An illustration for the mapping property shown in Eq. (14). Crossed lines indicate the branch cuts for  $\sqrt{(\omega/c - Mk_x)^2 - k_x^2}$ . Points A, B, and C have coordinates  $(M - 1)k_x$ ,  $(1 + s)Mk_x$ , and  $(M + 1)k_x$ , respectively, on the real axis. Point D represents an arbitrary point in the upper half  $\omega$  plane.

### III. Analysis of reflection coefficients

We will examine the potential benefits of the TIMIBC-ext for improving the accuracy of the TIMIBC by comparing the theoretical reflection coefficients at a liner surface produced by both conditions, as well as that by the original Ingard-Myers condition. Let a plane wave incident onto a lined surface located at  $z = 0$  be denoted as

$$p_{inc} = A_{inc} e^{ik_x x + ik_z z - i\omega t} \quad (16)$$

where for acoustic waves we have[8]

$$k_x = \left(\frac{\omega}{c}\right) \frac{\cos \theta}{1 + M \cos \theta}, \quad k_z = \left(\frac{\omega}{c}\right) \frac{\sin \theta}{1 + M \cos \theta}. \quad (17)$$

Here,  $\theta$  is the angle between the plane wave vector  $(k_x, k_z)$  and the  $x$  axis on the  $x$ - $z$  plane, as illustrated in Fig. 2. Note that in the current definition  $\theta$  is between  $-\pi$  and 0 for incident waves. With the angle  $\theta$  as defined in Fig. 2, the incident wave is in the downstream direction when  $-\pi/2 < \theta < 0$  and this situation will be referred to as Downstream Incidence (DI)/Upstream Source (US). The incident wave is in the upstream direction when  $-\pi < \theta < -\pi/2$  and this will be referred to as Upstream Incidence (UI)/Downstream Source (DS). At  $\theta = -\pi/2$ , the wave is at normal incidence.

Let the reflected wave be denoted by

$$p_{ref} = R A_{inc} e^{ik_x x - ik_z z - i\omega t}, \quad (18)$$

where  $R$  stands for the reflection coefficient.

Using the Ingard-Myers condition (Eq. 1), it is straightforward to find that  $R$ , when expressed in incidence angle  $\theta$ , is (see, e.g., [1, 6])

$$R = \frac{Z(1 + M \cos \theta) \sin \theta + \rho_0 c}{Z(1 + M \cos \theta) \sin \theta - \rho_0 c}. \quad (19)$$

On the other hand, the plane wave reflection coefficient given by the TIMIBC-ext (Eq. 7), denoted by  $R'$ , is found to be

$$R' = \frac{Z(1 + M \cos \theta) \sin \theta + \rho_0 c [1 + (1 - s)M \cos \theta - sM^2 \cos^2 \theta]}{Z(1 + M \cos \theta) \sin \theta - \rho_0 c [1 + (1 - s)M \cos \theta - sM^2 \cos^2 \theta]}. \quad (20)$$

Compared with Eq. (19), it is easy to see that the difference between  $R$  and  $R'$  is caused by an extra term  $\delta$ ,

$$\delta = (1 - s)M \cos \theta - sM^2 \cos^2 \theta, \quad (21)$$

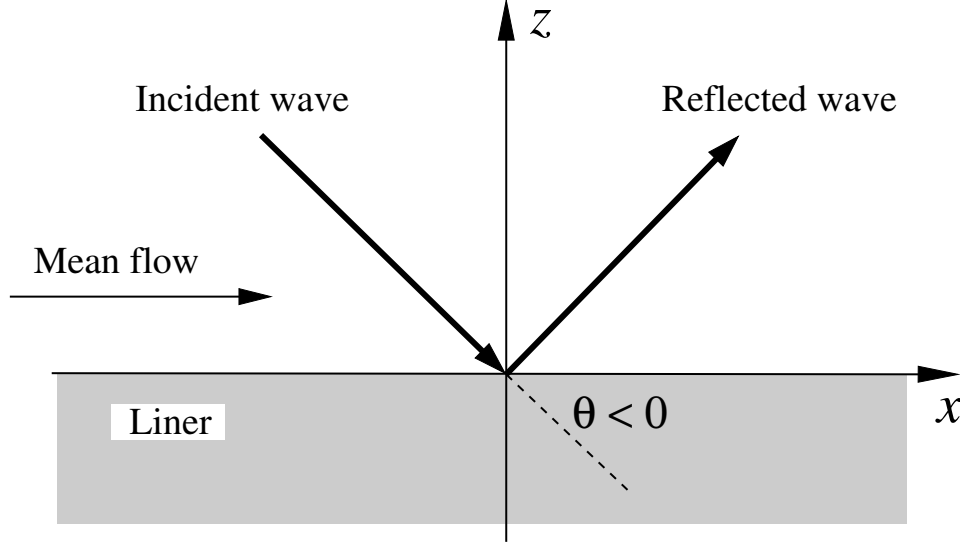


**Figure 2** A schematic diagram showing a plane wave incident onto a liner surface at  $z = 0$ .

that appears in both the numerator and denominator of Eq. (20). We observe that, while this difference term  $\delta$  is always zero for normal incident waves (i.e.,  $\theta = -\pi/2$ ), it can be made to vanish for an additional angle  $\theta_0$ , called the vanishing angle, when the tunable parameter  $s$  is such that

$$(1 - s) - sM \cos \theta_0 = 0. \quad (22)$$

This yields

$$s = \frac{1}{1 + M \cos \theta_0}. \quad (23)$$

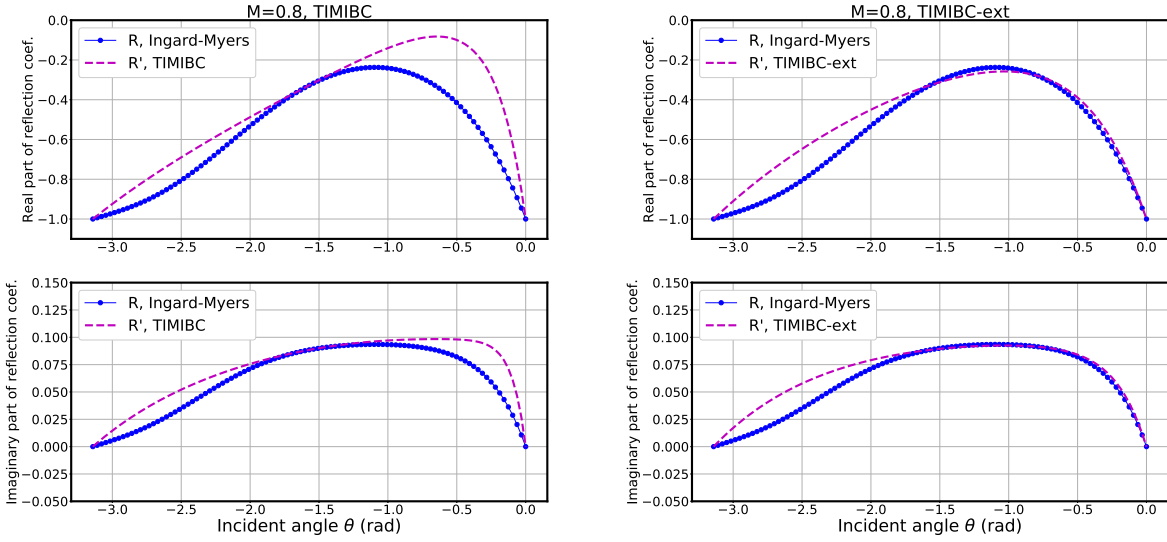
For a subsonic flow ( $|M| < 1$ ), to satisfy condition (9) for  $s$ , the vanishing angle  $\theta_0$  should be such that

$$\frac{M}{1 + M \cos \theta_0} < 1. \quad (24)$$

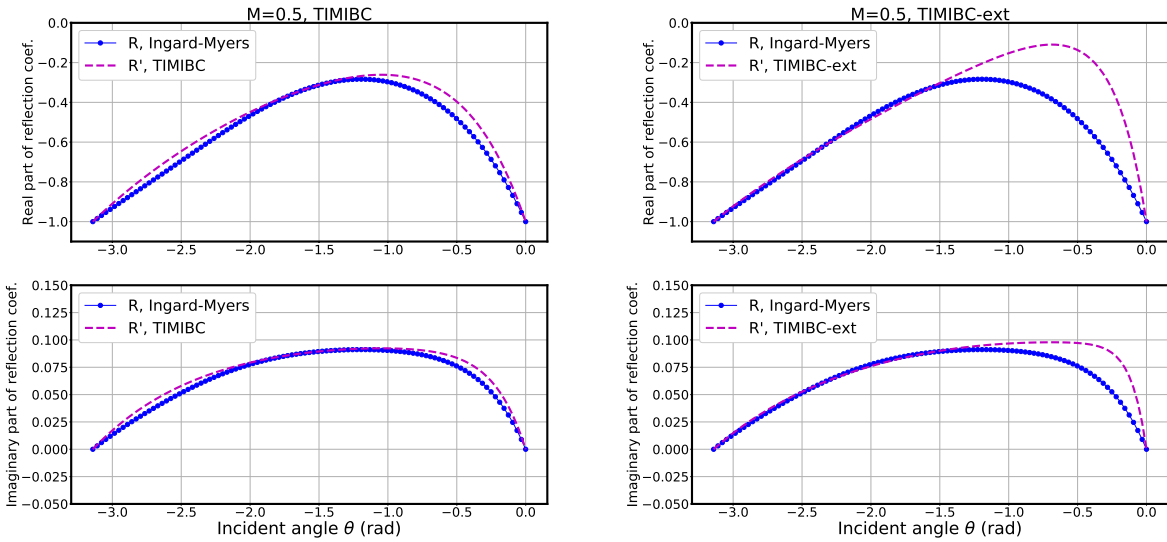
To show the benefits of choosing a proper value for parameter  $s$ , the reflection coefficients for the TIMIBC-ext (Eq. 20) and the TIMIBC (Eq. 20,  $s = 1$ ), and their comparisons with that by the Ingard-Myers condition (Eq. 19) are plotted in Fig. 3, using  $M = 0.8$  and  $Z/\rho_0 c = 0.5 + 0.1i$ . For the results shown in Fig. 3, the vanishing angle  $\theta_0$  for the parameter  $s$  as shown in Eq. (23) is chosen to be  $-\pi/4$ , a downstream incident angle. It is seen that, at such a high subsonic Mach number, the reflection coefficient by the TIMIBC differs substantially from that by the Ingard-Myers condition, except near the angle of normal incidence,  $\theta = -\pi/2$ , where the two match exactly. On the other hand, the differences between the TIMIBC-ext and the Ingard-Myers are drastically reduced for all the downstream incident angles. In fact, it is found that the improvement in the reflection coefficient is not sensitive to the particular choice of  $\theta_0$  as long as it is an angle within the downstream incidence range. This demonstrates the potential of the TIMIBC-ext for improving the performance of the TIMIBC as a stabilized impedance condition for flows with a high subsonic Mach number.

Figure 4 shows the comparison of reflection coefficients when the vanishing angle  $\theta_0$  is chosen to be an upstream incident angle. For the choice of  $\theta_0 = -3\pi/4$ , with  $M = 0.5$  and  $Z/\rho_0 c = 0.5 + 0.1i$ , the errors in the reflection coefficient are clearly reduced for all the upstream incident waves,  $-\pi < \theta < -\pi/2$ . However, the errors for the downstream incident waves, for which  $-\pi/2 < \theta < 0$ , are seen to be increased as a result. This implies choosing an upstream vanishing angle would be beneficial only when the incident waves are expected to be initiated downstream of the liner.

Figure 5 shows the valid choices of vanishing angle  $\theta_0$  for a given mean flow Mach number  $M > 0$ . The solid curve in the figure indicates the limiting condition  $\cos \theta_0 = (M - 1)/M$  as given by Eq. (24). The valid values for  $\theta_0$  are to the right of the curve when  $M > 0.5$  while no such limit is necessary when  $M \leq 0.5$ . The vertical dashed line denotes



**Figure 3** Comparison of reflection coefficients between  $R$  by the Ingard-Myers condition and  $R'$  by the TIMIBC on the left, and between  $R$  and  $R'$  by the TIMIBC-ext on the right, where  $\theta$  is the plane wave incident angle. The incident wave is in the downstream direction when  $-\pi/2 < \theta < 0$  and upstream when  $-\pi < \theta < -\pi/2$ . For the TIMIBC-ext, the vanishing angle  $\theta_0 = -\pi/4$ .



**Figure 4** Comparison of reflection coefficients between  $R$  by the Ingard-Myers condition and  $R'$  by the TIMIBC on the left, and between  $R$  and  $R'$  by the TIMIBC-ext on the right, where  $\theta$  is the plane wave incident angle. The incident wave is in the downstream direction when  $-\pi/2 < \theta < 0$  and upstream when  $-\pi < \theta < -\pi/2$ . For the TIMIBC-ext, the vanishing angle  $\theta_0 = -3\pi/4$ .

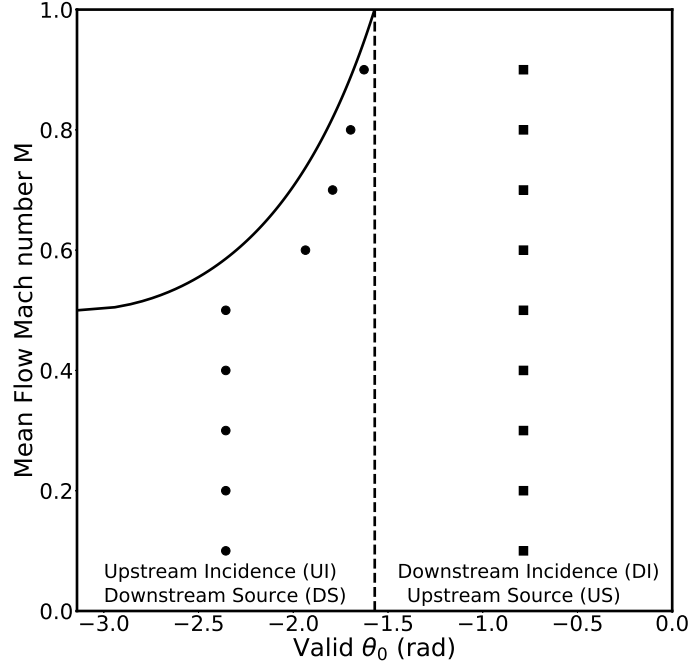


**Figure 5** Valid choices of vanishing angle  $\theta_0$  for a given mean flow Mach number  $M > 0$ . The solid curve indicates  $\cos \theta_0 = (M - 1)/M$ . The valid values for  $\theta_0$  are to the right of the curve. The solid circles and square symbols indicate the choices of  $\theta_0$  for the value of  $s$  as defined in Eq. (23) used in generating the results shown in Fig. (6). The vertical dashed line denotes the separation of valid upstream and downstream vanishing angles.

the separation of valid upstream and downstream vanishing angles. The vanishing angle is in the downstream direction (Upstream Source) when  $-\pi/2 < \theta_0 < 0$  and upstream direction (Downstream Source) when  $-\pi < \theta_0 < -\pi/2$ .

Figure 6 shows the effect of Mach number on the errors of the reflection coefficients for the TIMIBC-ext when the parameter  $s$  is determined by Eq. (23). Let  $E_{US}$  and  $E_{DS}$  respectively denote the difference between  $R$ , Eq. (19), and  $R'$ , Eq. (20), averaged over all downstream incident (Upstream Source) and upstream incident (Downstream Source) angles, i.e.,

$$E_{US} = \frac{2}{\pi} \int_{-\pi/2}^0 |R - R'| d\theta, \quad (25)$$

$$E_{DS} = \frac{2}{\pi} \int_{-\pi}^{-\pi/2} |R - R'| d\theta. \quad (26)$$

Plotted in Fig. 6(a) are the maximum  $E_{US}$  over a range of all impedance values of  $Z = Z_r + iZ_i$  for  $0 < Z_r/\rho_0 c \leq 10$  and  $-10 \leq Z_i/\rho_0 c \leq 10$ , where a grid search is conducted. The parameter  $s$  is chosen with a downstream incident angle  $\theta_0 = -\pi/4$  (closed squares in Fig. 5). Significant reduction of the differences by the TIMIBC-ext over the TIMIBC is observed for all Mach numbers.

For upstream incidence (Downstream Source), due to the condition given in (24), the choice for the vanishing angle  $\theta_0$  is restricted when  $|M| > 0.5$ . Plotted in Fig. 6(b) are the maximum  $E_{DS}$  when the parameter  $s$  is chosen with an upstream incident angle (closed circles in Fig. 5)

$$\theta_0 = \begin{cases} -3\pi/4 & 0 < M \leq 0.5 \\ -\pi/4 + \theta_M/2 & 0.5 < M < 1 \end{cases}, \quad (27)$$

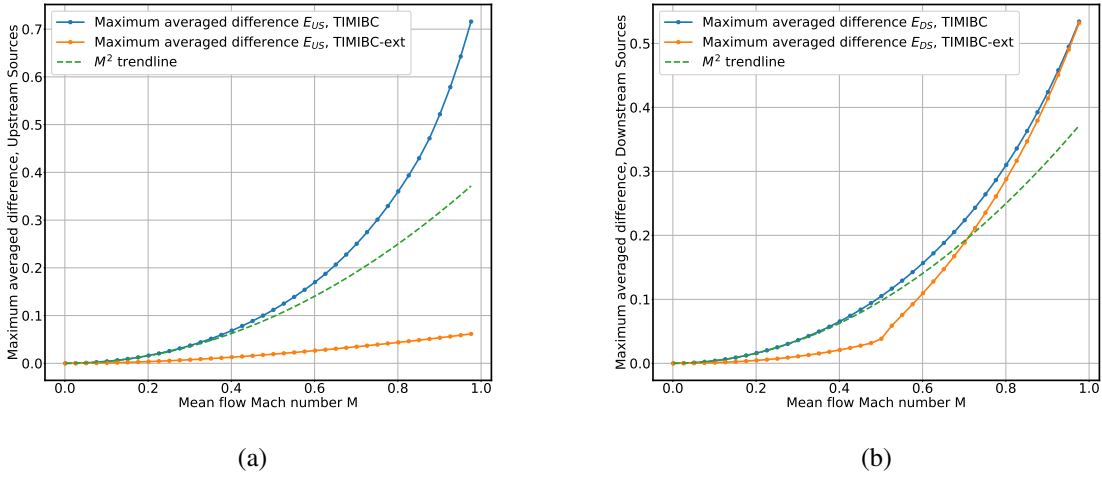


**Figure 6** Error of reflection coefficients as a function of Mach number  $M$  averaged over (a) all downstream incident angles, Eq. (25), and (b) all upstream incident angles, Eq. (26).

in which

$$\theta_M = -\arccos\left(\frac{M-1}{M}\right). \quad (28)$$

The reflection error is significantly reduced up to around  $M = 0.5$  in Fig. 6(b). As expected, for upstream incidences/downstream sources, the benefit of the TIMIBC-ext over the TIMIBC decreases as the Mach number increases from 0.5, unlike the case for the downstream incidences/upstream sources shown in Fig. 6(a). This is due to the limitation for the choice of the vanishing angle  $\theta_0$  as shown in Fig. 5.

In summary, choosing a vanishing angle  $\theta_0$ , hence the value of  $s$  by Eq. (23), for a downstream incidence angle reduces the error in the reflection coefficient for waves at all downstream incidence angles. Therefore, we may simply choose  $\theta_0 = -\pi/4$  for the case of Downstream Incidence/Upstream Source, resulting in a value for  $s$  as

$$\text{Downstream Incidence/Upstream Source} : s = \frac{1}{1 + M/\sqrt{2}}. \quad (29)$$

Similarly, for the case of Upstream Incidence/Downstream Source, we may simply choose  $\theta_0$  as given in Eq. (27), resulting in a value for  $s$  as

$$\text{Upstream Incidence/Downstream Source} : s = \begin{cases} \frac{1}{1-M/\sqrt{2}} & 0 < M \leq 0.5 \\ \frac{1}{1-\sqrt{M}(1-\sqrt{2M-1})/2} & 0.5 < M < 1 \end{cases}. \quad (30)$$

These choices for the vanishing angle  $\theta_0$  are as shown in Fig. (5). Of course, if only incident waves of a single angle are considered, the vanishing angle  $\theta_0$  can be set to that angle, and the value of  $s$  is then determined by Eq. (23) accordingly.

#### IV. Time domain impedance boundary condition for TIMIBC-ext

In this section, we discuss the implementation of the TIMIBC-ext in time domain simulations. Let the impedance, as a function of frequency, be expressed as the following multipole expansion[9–13]:

$$Z(\omega) = -i\omega h_0 + R_0 + \sum_{m=1}^N \frac{A_m}{\lambda_m - i\omega} + \frac{1}{2} \sum_{\ell=1}^L \left[ \frac{B_\ell + iC_\ell}{\alpha_\ell + i\beta_\ell - i\omega} + \frac{B_\ell - iC_\ell}{\alpha_\ell - i\beta_\ell - i\omega} \right]. \quad (31)$$

This will be referred to as the broadband multipole expansion model. It contains  $N + 2L$  poles in the complex  $\omega$ -plane. In Eq. (31), all parameters  $h_0, R_0, \lambda_m, A_m, \alpha_\ell, \beta_\ell, B_\ell, C_\ell$  assume real values. The values of these parameters are to be determined such that  $Z(\omega)$  matches the measured impedance values as closely as possible. For such a model to be physical, the function  $Z(\omega)$  should satisfy the conditions for causality, reality, and passivity [4, 14, 15], or be a *positive-real* function as defined in [16]:

- 1) (Causality)  $Z(\omega)$  is analytic (no poles) in open upper half-plane  $Im\{\omega\} > 0$ ;
- 2) (Reality)  $\bar{Z}(\omega) = Z(-\omega)$  for real  $\omega$  (an overbar denotes complex conjugate);
- 3) (Passivity)  $Re\{Z(\omega)\} \geq 0$  for  $Im\{\omega\} \geq 0$ .

These conditions lead immediately to the requirements that [16, 17]:

$$h_0, R_0, \lambda_m, \alpha_\ell \geq 0. \quad (32)$$

A minimization procedure written in Python for finding the coefficients of the multipole expansion ensuring passivity has recently been formulated in [6]. Time domain implementation of the TIMIBC-ext using the multipole expansion (Eq. 31) is given below.

### A. Time domain impedance boundary for pressure and its normal derivative

Applying Eq. (31) to the TIMIBC-ext condition (Eq. 7), it is straightforward to find the following time domain formulation for  $p$  and  $\partial p/\partial n$ :

$$h_0 \frac{\partial p_n}{\partial t} + R_0 p_n = -\rho_0 \left( \frac{\partial p}{\partial t} + (1+s)U \frac{\partial p}{\partial x} \right) - \sum_{m=1}^N A_m p_m^{(0)} - \sum_{\ell=1}^L \left[ B_\ell p_\ell^{(1)} + C_\ell p_\ell^{(2)} \right], \quad (33)$$

$$\frac{dp_m^{(0)}}{dt} + \lambda_m p_m^{(0)} = p_n, \quad m = 1, \dots, N, \quad (34)$$

$$\frac{dp_\ell^{(1)}}{dt} + \alpha_\ell p_\ell^{(1)} + \beta_\ell p_\ell^{(2)} = p_n, \quad \frac{dp_\ell^{(2)}}{dt} + \alpha_\ell p_\ell^{(2)} - \beta_\ell p_\ell^{(1)} = 0, \quad \ell = 1, \dots, L, \quad (35)$$

where  $p_n$  stands for the normal pressure derivative term  $\partial p/\partial n$ , and  $p_m^{(0)}$  and  $p_\ell^{(1)}, p_\ell^{(2)}$  are auxiliary variables that are introduced for the convenience of implementation in which,  $m = 1, \dots, N$  and  $\ell = 1, \dots, L$ .

### B. Time domain impedance boundary for normal acoustic velocity

The frequency domain TIMIBC-ext (Eq. 7) written in terms of pressure  $p$  and normal velocity  $u_n$  at the boundary can be expressed as follows:

$$(-i\omega) \hat{p} + (1+s)U \frac{\partial \hat{p}}{\partial x} = Z \left( (-i\omega) \hat{u}_n + U \frac{\partial \hat{u}_n}{\partial x} \right). \quad (36)$$

Converting into the time domain, we obtain the following boundary condition written in a system of first-order differential equations for computing  $u_n$  at lined boundary points:

$$h_0 \frac{\partial u_n}{\partial t} + R_0 u_n = p + sU \frac{\partial g}{\partial x} - \sum_{m=1}^N A_m p_m^{(0)} - \sum_{\ell=1}^L \left[ B_\ell p_\ell^{(1)} + C_\ell p_\ell^{(2)} \right], \quad (37)$$

$$\frac{dp_m^{(0)}}{dt} + \lambda_m p_m^{(0)} = u_n, \quad m = 1, \dots, N, \quad (38)$$

$$\frac{dp_\ell^{(1)}}{dt} + \alpha_\ell p_\ell^{(1)} + \beta_\ell p_\ell^{(2)} = u_n, \quad \frac{dp_\ell^{(2)}}{dt} + \alpha_\ell p_\ell^{(2)} - \beta_\ell p_\ell^{(1)} = 0, \quad \ell = 1, \dots, L, \quad (39)$$

$$\frac{\partial g}{\partial t} + U \frac{\partial g}{\partial x} = p, \quad (40)$$

where  $g, p_m^{(0)}$  and  $p_\ell^{(1)}, p_\ell^{(2)}$  are auxiliary variables in which,  $m = 1, \dots, N$  and  $\ell = 1, \dots, L$ .

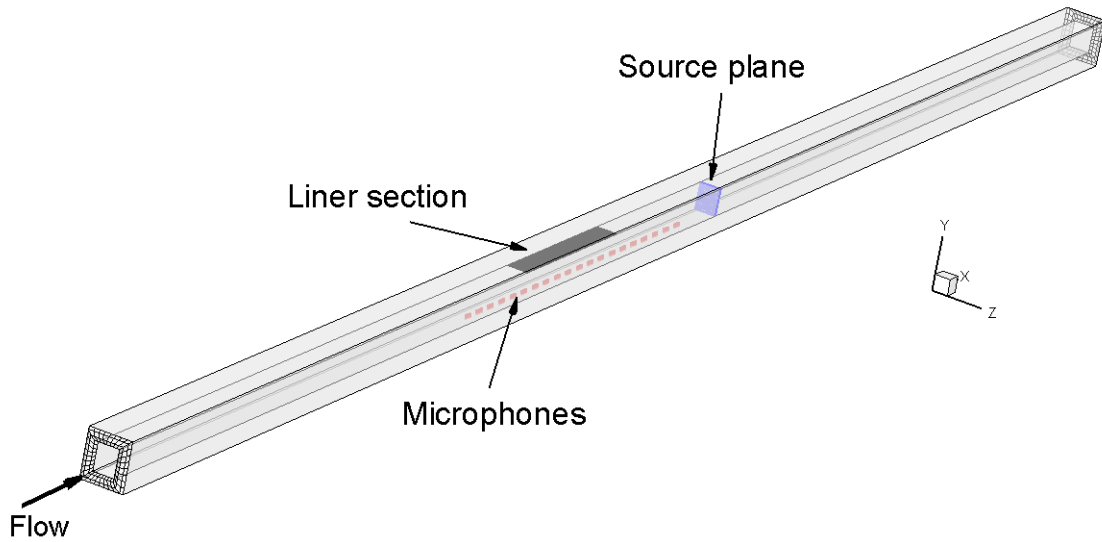


**Figure 7** A schematic diagram for the geometrical modeling of an internal ducted environment as an external scattering problem. The liner section inside the duct is noted by the darkened area. The dashed line indicates the locations of microphone measurements in the GFIT experiment. The location of the source plane where the incident mode is introduced is indicated by the square inside the duct.

## V. A numerical example

In this section, a numerical example is presented where a recent NASA Langley Research Center Grazing Flow Impedance Tube (GFIT) experiment[7] is simulated using the TIMIBC-ext condition. In order to formulate the numerical simulation as an external scattering problem, the inherently internal duct propagation problem is cast in an open-ended duct configuration. A duct geometry is constructed where part of its surfaces reproduce the ducted environment in the GFIT experiment while external and terminating surfaces are added such that a closed scattering body surface is formed, as shown in Figure 7.

The following convective wave equation of a uniform mean flow  $\mathbf{U}$  is solved by a time domain boundary element method:

$$\left( \frac{\partial}{\partial t} + \mathbf{U} \cdot \nabla \right)^2 p - c^2 \nabla^2 p = s(\mathbf{r}, t), \quad (41)$$

where  $\mathbf{r} = (x, y, z)$  is the position vector,  $t$  is time,  $c$  is the speed of sound, and  $s(\mathbf{r}, t)$  represents a prescribed acoustic source term. Here,  $\nabla = (\partial/\partial x, \partial/\partial y, \partial/\partial z)$ . In addition, the source function  $s(\mathbf{r}, t)$  in Eq. (41) is formulated such that an incident plane wave is generated in the ducted region. The time domain impedance boundary condition (Eqs. 33-35) is applied on a section of the duct interior surface where the acoustic liner is installed. In this way, propagation and scattering of the zeroth-order plane wave mode by the liner section are computed as a time domain scattering problem. The details of the numerical method are given in [5] and are not repeated here. We note that although the incident source is the zeroth-order plane wave mode, higher-order modes are present and observed in the numerical solution for the acoustic field due to scattering by the liner. The acoustic field produced by the computation will be compared to measured data from the aforementioned GFIT experiment[7]. While multiple liners were considered in the experimental study, only the results for the liner labeled IU2 are included in this work. The IU2 liner is a 15.5"-long perforate-over-honeycomb liner additively manufactured using stereolithography (SLA) resin, and consists of a 4×30 array of 0.4"×0.4"×2.0" chambers with an integrated facesheet. There are 22 perforations with a diameter of 0.041" positioned over each chamber such that they do not interface with the 0.13"-thick solid partitions that separate the chambers. As discussed further in the description of the GFIT test campaign [7], the liner was designed to be weakly nonlinear with a facesheet thickness of 0.034".

### A. Formulation of incident plane wave

To impose an incident plane wave (zeroth order mode) inside the duct as in the GFIT experiments, the source term for the wave equation (Eq. 41) is specified as the following:

$$s(\mathbf{r}, t) = \Phi_0'(t)\delta(x - x_0), \quad (y, z) \in [0, L_y] \times [-L_z/2, L_z/2], \quad (42)$$

where  $\Phi_0(t)$  is a prescribed function of  $t$  and a prime denotes the derivative with respect to  $t$ ,  $x_0$  is the  $x$ -coordinate for the location of the source (referred to as the source plane, where the plane wave is to be introduced), and  $L_y$  and  $L_z$  denote the dimensions of the duct cross section in  $y$  and  $z$  directions, respectively. For the results reported in this section, the boundary element model for the duct extends from  $x = -1.5$  to  $x = 3.0$ . Throughout this example, the length unit is meters (m) and the duct cross section is such that  $L_y = 0.0635$  and  $L_z = 0.0508$  as used in the GFIT experiment. A liner section is installed at the upper surface of the duct from  $x = 0.208$  to  $x = 0.615$  and at  $y = L_y$ . Solving the wave equation (Eq. 41) with a source term given in Eq. (42), it can be shown that the analytical solution for the acoustic pressure  $p(\mathbf{r}, t)$  generated inside a duct of solid surfaces is a plane wave pulse of the form

$$p(\mathbf{r}, t) = \begin{cases} \Phi_0\left(t - \frac{x-x_0}{U+c}\right) & x > x_0 \\ \Phi_0\left(t - \frac{x-x_0}{U-c}\right) & x < x_0 \end{cases}, \quad (y, z) \in [0, L_y] \times [-L_z/2, L_z/2]. \quad (43)$$

Equation (43) represents two *independent* plane waves (zeroth order mode) propagating at a speed of  $U + c$  and  $U - c$  to the right and left, respectively, of the source plane location  $x = x_0$ . Here,  $U$  is the streamwise uniform mean flow velocity inside the duct.

For the current computation, the source time function in Eq. (42) is taken to be the following broadband Gaussian function:

$$\Phi_0(t) = e^{-\sigma t^2} \quad (44)$$

where  $\sigma = 1.42/(6\Delta t)^2$ , where  $\Delta t$  is the time step used in the numerical simulation. Since the plane waves will eventually be reflected at the ends of the duct, the time domain simulation is to be stopped before the reflected waves reach the microphones located at the side of the duct opposite to the liner section from  $x = 0$  to  $x = 1$ . For this purpose, the source plane location is  $x_0 = 1.1$ , downstream of the liner section and sufficiently away from the trailing edge of the liner section and the microphone locations.

### B. Numerical results and comparison with experimental data

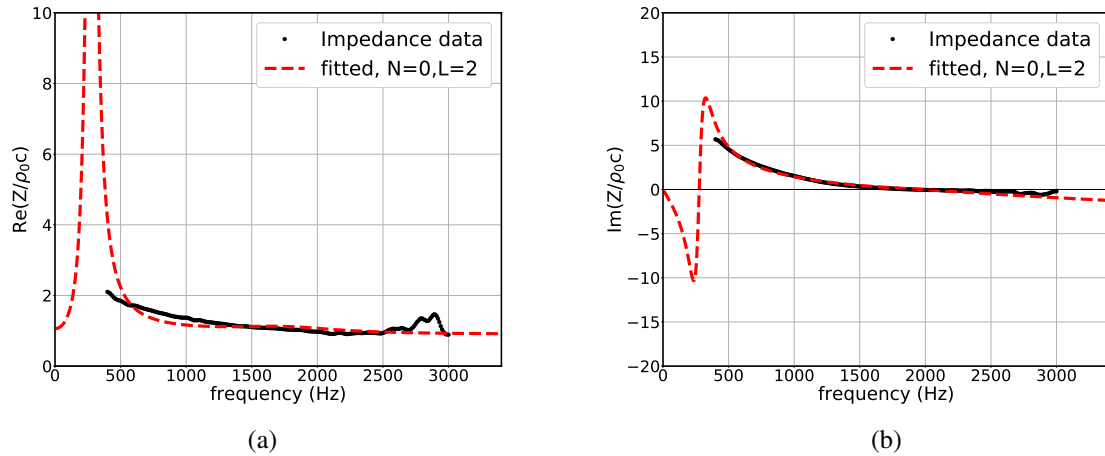
In the GFIT experiment that is used in the current comparison[7], the mean flow is non-uniform with a setpoint centerline Mach number of 0.6. However, for the computational results reported here, a uniform mean flow Mach number of 0.433, the average velocity measured in the experiment, is assumed because a constant mean flow is required for the boundary integral equation formulation[5]. In the experiment, microphones are mounted on the lower wall ( $y = 0$ ) opposite the liner section from  $x = 0$  to  $x = 1$  to measure the pressure field. Based on the experimental measurements, the impedance of the liner is educed at a set of discrete frequencies from 400 Hz to 3000 Hz, with an increment of 10 Hz, resulting in a set of impedance values for 261 frequencies.

For the IU2 liner considered here, the educed resistance and reactance are plotted as discrete points in Fig. 8. The educed impedance is numerically simulated using the multipole expansion model (Eq. 31) with a simple choice of two paired poles, i.e.,  $N = 0$  and  $L = 2$ . The multipole expansion approximation is plotted as dashed lines in Fig. 8. The coefficients for the expansion, normalized by  $\rho_0 c$ , are as follows:

$$\begin{aligned} h_0 &= 0.029796, \quad R_0 = 0.893594, \\ \alpha_1 &= 9.571242, \quad \beta_1 = 32.883047, \quad B_1 = 3.133092, \quad C_1 = 0.729854, \\ \alpha_2 &= 0.838532, \quad \beta_2 = 5.042585, \quad B_2 = 34.902352, \quad C_2 = -5.176662. \end{aligned}$$

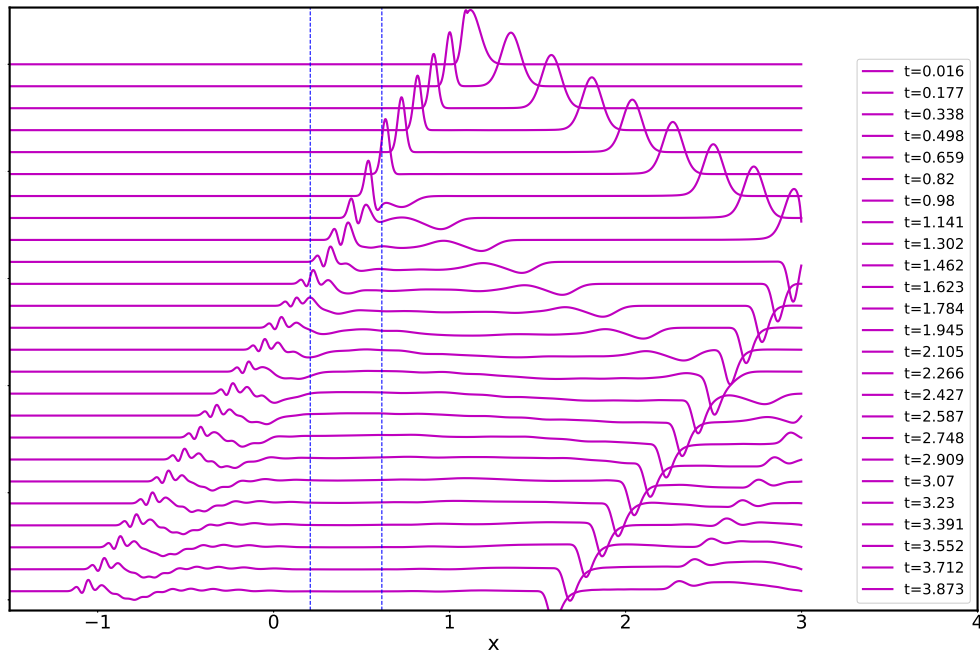
The multipole expansion model fits the educed impedance relatively well over the full range of frequencies over which measurements were made. This allows the liner effects at all frequencies to be simulated in a single time domain calculation using the model.

Figure 9 shows stacked snapshots of pressure variation along the duct interior surface opposite the liner section. As the plane wave pulse propagates to the left of the source location, the effects of the liner on the incident pressure pulse are clearly seen and captured by the computation. Mean flow effect on the width of the upstream and downstream



**Figure 8** Multipole expansion approximation of impedance function. Symbols are the experimentally educed values and dashed lines are values by the fitted model. (a) Resistance; (b) Reactance.

propagating pulses is evident in Fig. 9. Also visible are the reflections of the plane wave pulses by the trailing edge of the liner section and by the terminating opening of the duct at  $x = 3$ . The time domain simulation is stopped before the wave reflected from the end of the duct reaches the measurement zone from  $x = 0$  to  $x = 1$ .



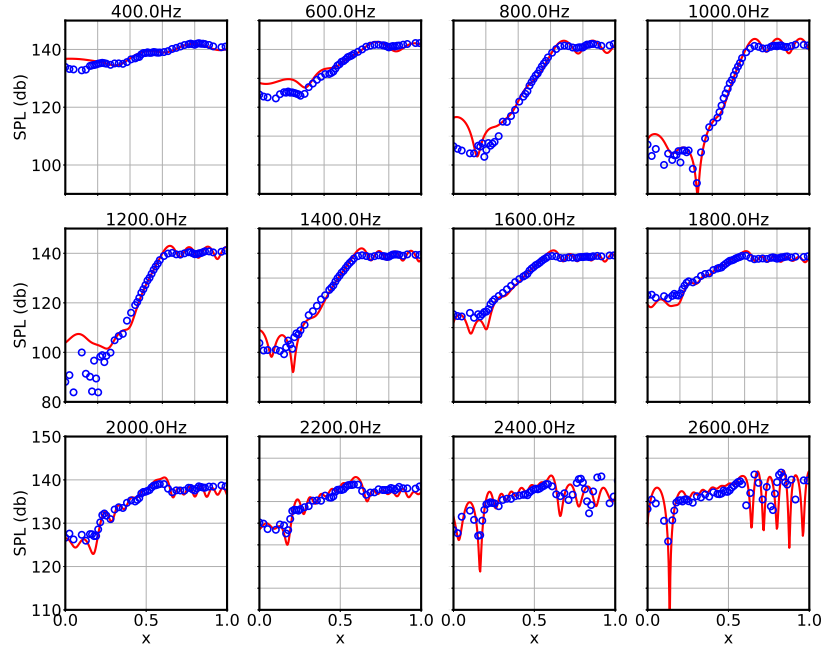
**Figure 9** Stacked snapshots of acoustic pressure along the ducted side-wall opposite to the side of the liner at selected times as indicated. A broadband plane wave is introduced downstream of the liner section. Vertical dotted lines indicate the leading and trailing edges of the liner section.

The time domain solution is converted into the frequency domain using the Fourier transform. Due to space limitations, we cannot show the comparison for all 261 frequencies. Figure 10 presents the comparison of computed and experimental results at a set of selected frequencies for the pressure distribution along the wall opposite the liner section. The distribution of sound pressure level (SPL) and phase is plotted in Fig. 10(a) and Fig. 10(b), respectively. The symbols represent the measurements, and the lines depict the computations. Very good agreement is observed at all frequencies, both for the sound pressure level absorption and for the phase distributions. The deviations that appear in the comparisons between predicted and measured values in cases involving large attenuation (e.g., approximately 40 dB at  $x \lesssim 0.25$  m for frequencies from 800-1200 Hz) are largely due to the duration of the swept sine source used in the experiment. Increasing the swept sine duration would allow for more data averaging and reduced scatter in such situations (however, at the expense of increased measurement time). These comparisons demonstrate the validity of the TIMIBC-ext formulation as a time domain impedance boundary condition for lined surfaces with high speed grazing flow.

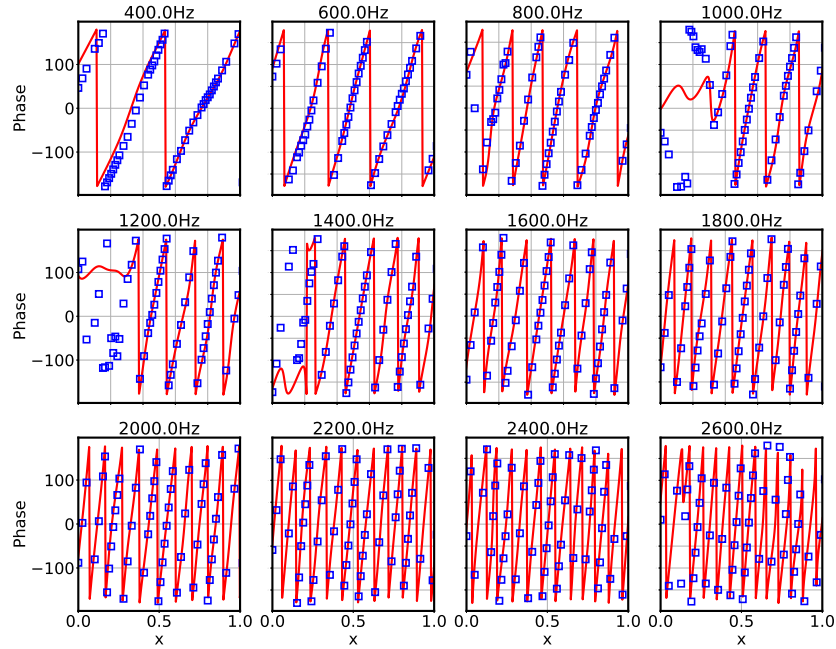
To compare the performances of the TIMIBC and the TIMIBC-ext, another simulation for the current configuration is conducted by applying the TIMIBC condition (Eqs. 33-35,  $s = 1$ ) on the liner surface. Figure 11 shows the SPL results for both conditions at two frequencies for which the predictions differ the most. It is evident that the solution provided by the TIMIBC-ext is closer to the measurements. Although a setpoint centerline velocity of Mach number 0.6 is only moderately high, we expect that the improvement by the TIMIBC-ext over the TIMIBC would be more significant for higher Mach numbers.

## VI. Conclusions

An extension of the recently proposed TIMIBC to liners with a grazing flow of high subsonic Mach numbers has been considered. While the TIMIBC effectively eliminates the Kelvin-Helmholtz-type instability inherent in the original Ingard-Myers condition, it only approximates the Ingard-Myers condition well at low to mid Mach numbers. The proposed TIMIBC-ext is a generalization of the TIMIBC with a tunable parameter. It has been found that the value for this parameter can be chosen to improve the accuracy of the TIMIBC for waves of either Upstream Incidence (UI)/Downstream Source (DS) or Downstream Incidence (DI)/Upstream Source (US). Consequently, the TIMIBC-ext would be an effective and stable time domain impedance condition for flows with high subsonic Mach numbers when the sound source location relative to the liner, either upstream or downstream, is known. A numerical example of the TIMIBC-ext has been presented using the NASA GFIT configuration, where the source is placed downstream of the liner. Comparison of computational results and experimental measurements has demonstrated the validity of the TIMIBC-ext.



(a)



(b)

**Figure 10 (a): SPL vs.  $x$  at selected frequencies as indicated; (b): Phase vs.  $x$ . Line: computation; Symbol: experiment.**

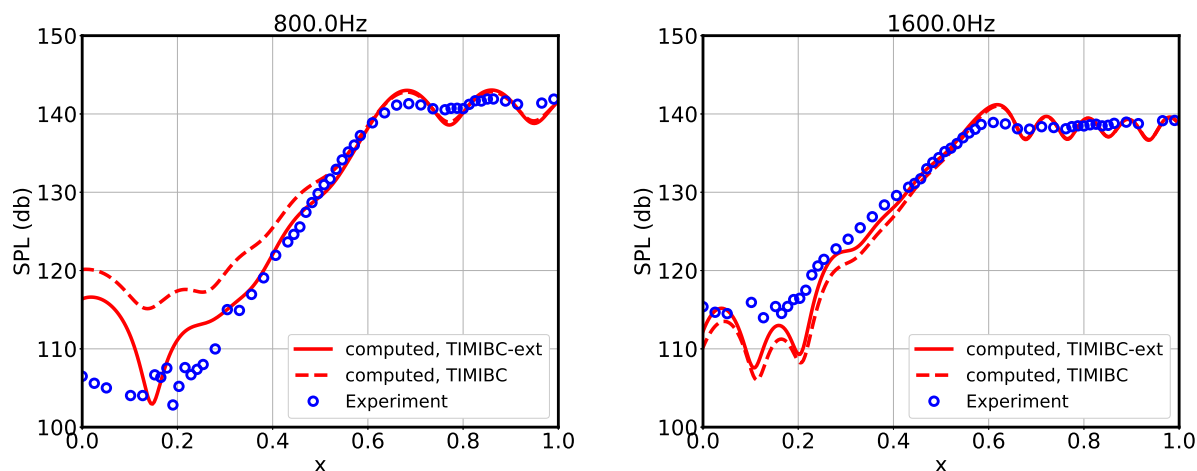


**Figure 11** Sound pressure level distributions computed by the TIMIBC and TIMIBC-ext and their comparison with GFIT measurements.

### Acknowledgments

This research was funded by NASA’s Advanced Air Transport Technology (AATT) Project and Revolutionary Vertical Lift Technology (RVLT) project. This work used the computational resources at the Old Dominion University ITS Turing cluster.

### References

- [1] Ingard, U., “Influence of fluid motion past a plane boundary on sound reflection, absorption, and transmission,” *Journal of the Acoustical Society of America*, Vol. 31, 1959, p. 1035.
- [2] Myers, M., “On the acoustic boundary condition in the presence of flow,” *Journal of Sound and Vibration*, Vol. 71, 1980, pp. 429–434.
- [3] Tester, B. J., “The propagation and attenuation of sound in lined ducts containing uniform or “plug” flow,” *Journal of Sound and Vibration*, Vol. 28, 1973, pp. 151–203.
- [4] Tam, C. K. W., and Auriault, L., “Time-domain impedance boundary conditions for computational aeroacoustics,” *AIAA Journal*, Vol. 34, 1996, pp. 917–923.
- [5] Hu, F. Q., and Nark, D. M., “On the Implementation and Further Validation of a Time Domain Boundary Element Method Broadband Impedance Boundary Condition,” AIAA Paper 2022-2898, 2022.
- [6] Hu, F. Q., and Nark, D. M., “On a stabilization of the Ingard-Myers impedance boundary condition,” AIAA Paper 2023-3342, also to appear in *International Journal of Aeroacoustics*, 2023.
- [7] Jones, M. G., Nark, D. M., and Howerton, B. M., “NASA Investigation of Flow Direction Effects on Impedance Education for Acoustic Liners,” AIAA Paper 2024-xxxx, to be published, 2024.
- [8] Morse, P. M., and Ingard, K. U., *Theoretical Acoustics*, 1<sup>st</sup> ed., Princeton University Press, Princeton, NJ, 1986.
- [9] Gustavsen, B., and Semlyen, A., “Rational approximation of frequency domain responses by vector fitting,” *IEEE Transactions on Power Delivery*, Vol. 14, 1999, pp. 1052–1061.
- [10] Reymen, Y., Baelmans, M., and Desmet, W., “Efficient implementation of Tam and Auriault’s time-domain impedance boundary condition,” *AIAA Journal*, Vol. 46, 2008, pp. 2368–2376.
- [11] Li, X. Y., Li, X. D., and Tam, C. K. W., “Improved Multipole Broadband and Time-Domain Impedance Boundary Condition,” *AIAA Journal*, Vol. 50, 2012, pp. 980–984.

- [12] Dagna, D., Pineau, P., and Blanc-Benon, P., "A Generalized Recursive Convolution Method for Time-Domain Propagation in Porous Media," *Journal of the Acoustical Society of America*, Vol. 138, 2015, pp. 1030–1042.
- [13] Chen, C., and Li, X. D., "Numerical efficiency analysis of multi-pole time-domain impedance boundary conditions," EUCASS 2019-1034, 2019.
- [14] Fung, K.-Y., and Ju, H., "Time-domain impedance boundary conditions for computational acoustics and aeroacoustics," *International Journal of Computational Fluid Dynamics*, Vol. 18, 2004, pp. 503–511.
- [15] Rienstra, S. W., "Impedance Models in Time-Domain Including the Extended Helmholtz Resonator Model," AIAA paper 2006-2686, 2006.
- [16] Brune, O., "Synthesis of a finite two-terminal network whose driving-point impedance is a prescribed function of frequency," *Journal of Mathematical Physics*, Vol. 10, 1931, pp. 191–236.
- [17] Chen, W.-K., *Passive, Active, and Digital Filters*, CRC Press, 2009.